HYDRODYNAMICS OF SLENDER UNDULATING FOIL

Li-Ming Chao
Center for Turbulence Control
Harbin Institute of Technology (Shenzhen)
University Town, Shenzhen, 518055, China
chaoliming92@gmail.com

Md. Mahbub Alam
Center for Turbulence Control
Harbin Institute of Technology (Shenzhen)
University Town, Shenzhen, 518055, China
alam@hit.edu.cn

ABSTRACT

The thrust generation and wake structures of a slender undulating foil have been studied, where the Strouhal number *St*, Reynolds number *Re* and dimensionless wavelength λ influences are considered. The relationship of time-mean thrust with *St*, *Re* and λ is presented, suggesting that the propulsive force increases with enlarging *St*, *Re* and λ. As such, the drag-thrust boundary advances with increasing them. Seven types of wake structures produced by the foil are identified, discussed, and connected to thrust generation, showing how *St*, *Re* and λ affect fluid dynamics, wake transition and vortex strength.

INTRODUCTION

After a long history of evolution, aquatic animals have mastered an exquisite capacity to control their body and the flow around themselves to efficiently cruise in water (Fish & Lauder, 2006). Slender swimmers, such as *anguilliform*, *carangiform* and *subcarangiform* swimmers, usually employ the undulating body-caudal-fin (BCF) propulsive strategy to propel themselves and overcome the fluid resistance, where the swimmers undulating BCF strategy can be considered as a combination of two waves. One is a cyclic change of the curved body producing a lateral wave propagation in the caudal direction, and the other is every single point on the body undergoing a sinusoidal track in a horizontal plane as the consequence of the wave propagation (Gray, 1933). For different slender swimmers, they may use different swimming strategies to bend their bodies. Even one specific swimmer has different deforming techniques at different conditions, such as the fish uses C-start deformation during the survival behavior (Gazzola *et al.*, 2012). However, to the authors knowledge, no systematic investigation has been made to understand the effect of deforming characteristics on the propulsive performance of an undulating swimmer. In this work, we, therefore, attempt to systematically investigate the hydrodynamic performance of an undulating foil with varying foil kinematics (Strouhal number), fluid properties (Reynolds number), and foil deforming characteristics (wavelength), with the foil length keeping constant to replicate the native slender swimmer.

PROBLEM DESCRIPTION

A schematic of the flow configuration is presented in figure 1(a), where a two-dimensional NACA0012 foil with chord-length of L is placed in a uniform flow of velocity U in the x-direction. The leading edge of the foil is located at the origin of the Cartesian coordinate system. The following equation is employed to control the foils undulation,

$$\begin{cases} y(x,t) = A(x)\sin\left[2\pi(\frac{x}{\lambda} - \frac{t}{T})\right] \\ \int_0^{L_s(t)} \sqrt{\{1+(\partial y/\partial x)^2\}}\,\mathrm{d}x = L \end{cases} \tag{1}$$

where $A(x)$ is the swimming amplitude function, usually considered as a polynomial $A(x) = a_0 + a_1 x + a_2 x^2$, x is measured from the leading edge of the foil, y is the lateral displacement of the foil midline, λ is the wavelength defined in figure 1(b), t is the instantaneous time, T is the undulating period, and $L_s(t)$ denotes projected length of the foil on the x-axis (streamwise direction), giving $L_s(t) \leq L$. Without a loss of generality, $a_0 = a_2 = 0$ and $a_1 = 0.05$ are employed to determine the foil undulation.

To follow the kinematics of a real swimmer, both the foil midline length and the included area are kept constant, with the foil midline computed from equation (1). The foil surface is given by maintaining the normal distance (e.g. h_s at an arbitrary point on the midline) from the midline constant for the deformed and undeformed foils. For example, consider that h_s is the distance between point A on the foil midline and point B (normal to the midline) on the foil surface when the foil is straight, undeformed (figure 1c). At each time step, the line AB normal to the deformed midline can be computed from the differential form of equation (1). The new location of point B on the foil surface is then pinpointed with AB = h_s. A typical envelope of the undulation is illustrated in figure 1(d), where it is easy to understand that $L_s(t)$ is a time-dependent variable, with $L_s(t) = L$ corresponding to the straight midline (dashed blue line), not undulating.

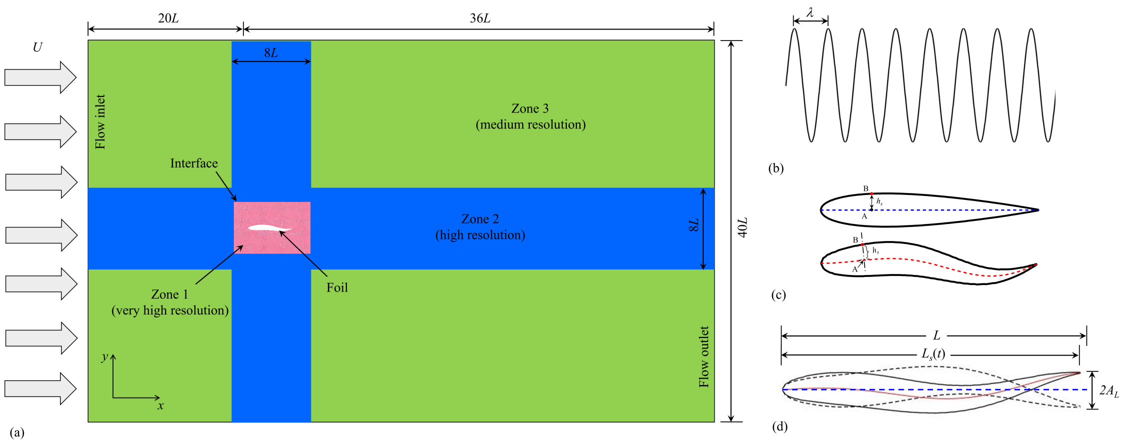

Figure 1. (a) Computational domain and mesh system, (b) traveling wavy motion, (c) method for achieving foil surface and (d) foil parameter.

Strouhal number and Reynolds number are defined as:

$$St = 2A_L/UT \tag{2}$$

and

$$Re = UL/\nu \tag{3}$$

where $A_L(=0.05L)$ is the tail amplitude and ν is the kinematic viscosity of the fluid. The time-mean thrust coefficient is defined as

$$\bar{C}_T = \frac{1}{T}\int_t^{t+T} C_T dt = \frac{1}{T}\int_t^{t+T} -\frac{F_x(t)}{0.5\rho U^2 L}dt \tag{4}$$

where C_T is the instantaneous thrust coefficient, $F_x(t)$ is the drag (x-direction) force acting on the foil, and ρ is the density of the fluid. Therefore, $\bar{C}_T > 0$ and $\bar{C}_T < 0$ represent the foil generating time-mean thrust and experiencing time-mean drag, respectively, while $\bar{C}_T = 0$ is the drag-thrust transition boundary.

NUMERICAL METHOD

The unsteady flow field around the foil is simulated using the commercially available CFD package Fluent 14.0. The flow domain consists of three grid zones, including a regular zone with a high resolution in unstructured grids around the foil (zone 1, figure 1a), zone 2 is of high resolution where a large velocity gradient is expected and zone 3 with a medium resolution. The locomotion of foil in the computational domain is achieved using a dynamic grid scheme implemented in FLUENT. At each updated time instant, the foil motion is determined using equation (1). The inlet velocity boundary is at a distance of 20L from the leading edge of the foil, with $\mathbf{u} = (U,0)$ and $\partial p/\partial x = 0$ while the outflow boundary is 36L downstream, with $\partial \mathbf{u}/\partial x = (0,0)$ and $\partial p/\partial x = 0$ (no-stress outflow boundary conditions). The slip wall condition is used for the upper and lower boundaries located symmetrically 40L apart (Bos *et al.*, 2008).

To investigate the thrust generation and wake structures of the slender undulating foil, the numerical simulations are performed at St = 0.1 1.0 with ΔSt = 0.1, at Re = 50, 100, 250, 500, 750, 1000, 1250, 1500, 1750, and 2000, and at λ = 0.50, 0.67, 1.0, 1.5 and 2.0.

THRUST GENERATION

Figures 2(a)-(e) illustrate the dependence of $\bar{C}_T$ on St, Re and λ. The solid black line represents the drag-thrust boundary ($\bar{C}_T = 0$). For a given λ, the $\bar{C}_T$ increases from negative (lower-left corner) to positive (upper right corner) when St and Re are increased. The traveling wavy foil cannot produce thrust when Re and St are low but can when Re and St are sufficiently high, depending on λ. Interestingly, $\bar{C}_T$ is equally dependent on St and Re in the drag regime ($\bar{C}_T < 0$) but more sensitive to St in the thrust regime ($\bar{C}_T > 0$). The observation indicates that viscous (Re) and inertia (St) effects both play important roles in fluid dynamics in the drag regime while the inertia effect dictates the fluid dynamics in the thrust regime. For a given set of St and Re, an increase in λ leads to an enhancement in $\bar{C}_T$. As such, the drag-thrust boundary shifts to the smaller St and Re when λ is increased. With the same St and λ, the $\bar{C}_T$ gets higher at a higher Re, i.e. having acceleration is easier at a higher speed. The reason is that the viscous effect weakens and the added mass lessens when Re is increased. On the other hand, a foil with a smaller λ hinders the streamwise flow over the surface, resulting in a smaller thrust generation.

When the stationary wavy foil ($St = 0$) remains traveling-wavy shape (as sketched in figure 2a-e), it would experience a thrust ($\bar{C}_{T0}$) that is negative (i.e. drag). Apparently, $\bar{C}_{T0}$ would dependent on Re as shown in figure 2(f), where declines with Re as $\bar{C}_{T0} = -6.13Re^{-0.6}$. Das *et al.* (2016) showed that a straight NACA0012 foil at zero attack angle incurs $\bar{C}_{T0} = -5.96Re^{-0.56}$ that is smaller in magnitude than the present counterpart. It is plausible as an undulated foil would experience a higher drag than a straight foil.

The linear least-squares regression is used to find the relationship between $\bar{C}_T$, St and λ, giving $\bar{C}_T = c_1 St^3\lambda + c_2$. After reprocessing the data obtained from the numerical simulations, the relationship of $\bar{C}_T$ with Re, St and λ can be unified as

$$\bar{C}_T = 0.36Re^{0.208}St^3\lambda - 6.13Re^{-0.6} \tag{5}$$

Equation (5) displays how St, Re, and λ affect the propulsive force on the foil. It is easy to understand from this equation that the thrust generation ($\bar{C}_T > 0$) is largely determined by St and λ, especially by St. The $\bar{C}_T$ enhances slowly with increasing Re, which essentially reflects the viscous flow resistance weakening with increasing Re. Particularly, when Re is large enough, the second term on the right-hand side approaches zero, which gives $\bar{C}_T = 0.36Re^{0.208}St^3\lambda$. When

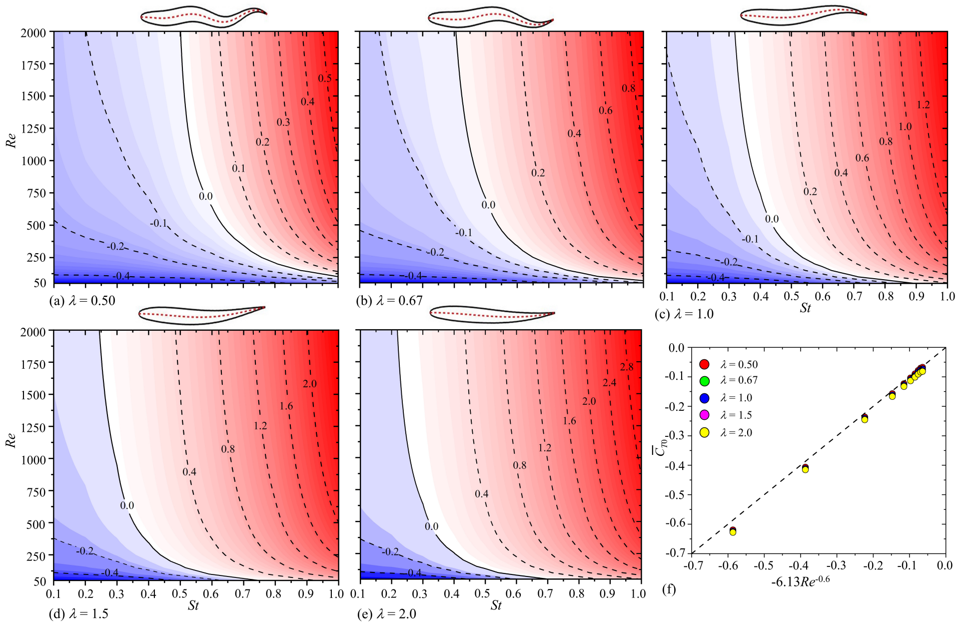

Figure 2. (a-e) Dependence of time-mean thrust on Re, St and λ for the undulating foil. (f) Dependence of time-mean thrust force of a stationary foil on Re.

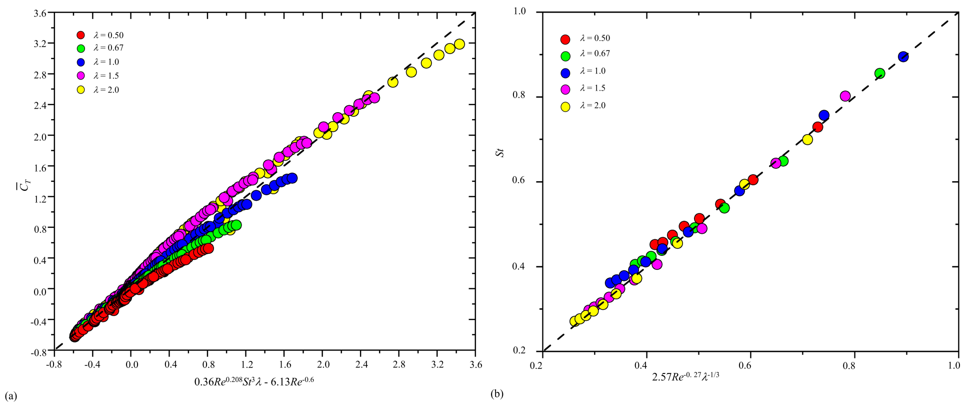

Figure 3. (a) Relationship of $\bar{C}_T$ with St, Re and λ for the undulating foil. (b) Dependence of drag-thrust boundary on St, Re and λ for the undulating foil. The dash lines denote the proportional function with a coefficient equal to one.

the foil is stationary ($St = 0$), equation (5) degenerates into $\bar{C}_T = -6.13Re^{-0.6}$, i.e. the $\bar{C}_{T0}$ scaling. To see how much equation (5) is capable of collapsing all simulated data, $\bar{C}_T$ is presented against $0.36Re^{0.208}St^3\lambda - 6.13Re^{-0.6}$ in figure 3(a).

The thrust generation is found to be dependent on λ. It is worth finding the relationship between St, Re, and λ corresponding to the drag-thrust boundary (figures 2a-e). The drag-thrust boundary can be obtained from equation (5) by plugging $\bar{C}_T = 0$, i.e.

$$St = 2.57Re^{-0.27}\lambda^{-1/3} \tag{6}$$

Equation (6) reflects that the drag-thrust boundary in the $St - Re$ domain advances with increasing λ, as illustrated in figure 3(b). The present results and relationship conform with the biological observations (Gazzola *et al.*, 2014) while the effect of the deforming strategy (λ) on the cruising locomotion is firstly presented in this work. Based on the theoretical model involving the Euler angular, Coriolis, and centrifugal accelerations of a cone of fluid around the foil, Alam & Muhammad (2020) theoretically showed that the relationship between $\bar{C}_T$ and St can be considered as $\bar{C}_T \propto St^3$.

Figure 4 displays C_T histories in one oscillation period at four selected points: A ($St = 0.2, Re = 100$) in drag regime, B ($St = 0.4, Re = 250$) close to the drag-thrust boundary at high λ, C ($St = 0.6, Re = 600$) close to the drag-thrust boundary at small λ, and D ($St = 0.8, Re = 1000$) in thrust regime, all marked in the $St - Re$ map (figure 2). Similar to the previous works on the pitching foil (Koochesfahani, 1989), two C_T peaks are observed in the upstroke and downstroke, respectively. The traveling wavy foil experiences drag during the entire period at $St = 0.2$, $Re = 100$ (figure 4a). For the given St and Re, the C_T peak becomes larger when λ increases from 0.50 to 2.0. At intermediate St and Re values (points B and C), the foil undergoes both drag and thrust in the period (figures 4b, c). On the other hand, at a higher St and Re, only thrust acts on the foil in the entire period (figure 4d). The C_T amplitude (the gap between maximum and minimum) grows with increasing St, Re and λ (figures 4a-d). A smaller λ, therefore, engenders a more steady thrust, which explains the swimming behavior of the anguilliform swimmer. On the other hand, the

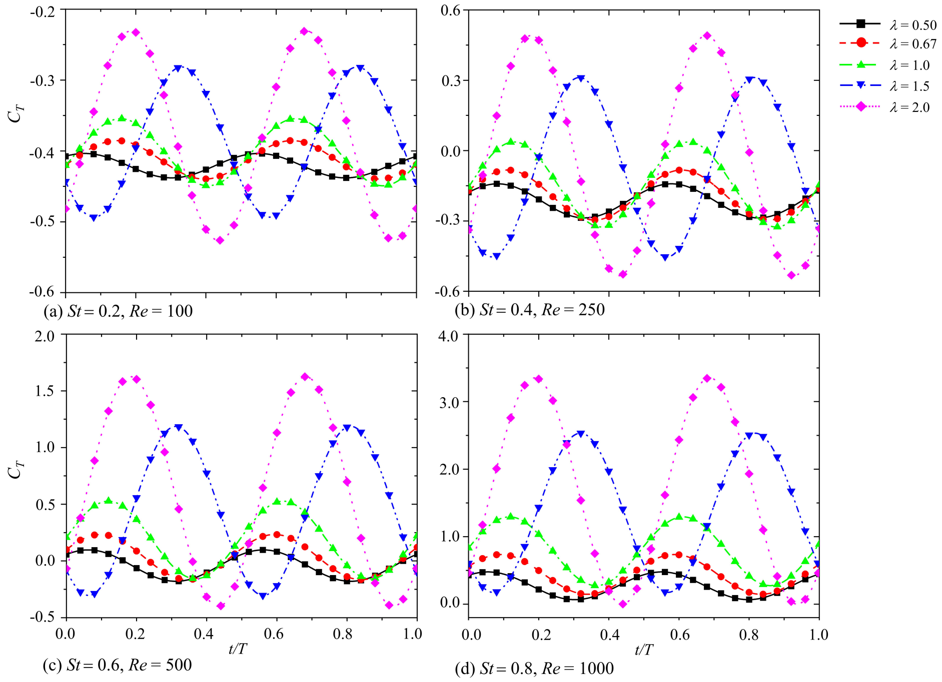

Figure 4. The instantaneous thrust coefficient for the traveling wavy foil in one oscillation period.

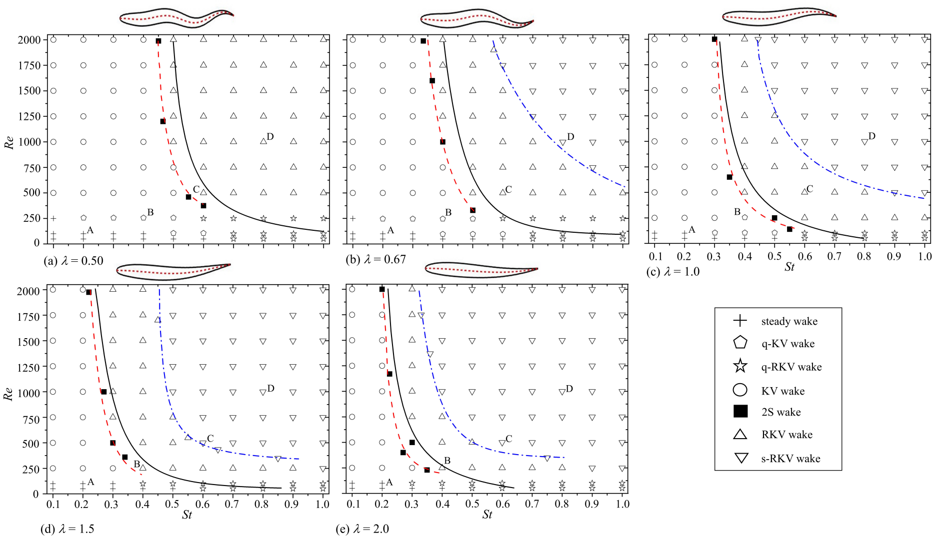

Figure 5. The wake structure map with the black solid line denoting the drag-thrust boundary, red dash line denoting the KV-RKV wake boundary and blue dash-dotted line denoting the RKV-s-RKV wake boundary.

maximum instantaneous thrust generated for a higher λ explicates why the slender swimmer usually employs the C-start strategy during the survival behavior (Gazzola *et al.*, 2012).

FLOW MAP

Seven distinguished wake structures are identified in the $St-Re$ domain examined: steady wake, quasi Kármán vortex (q-KV) wake, quasi reverse Kármán vortex (q-RKV) wake, Kármán vortex (KV) wake, 2S aligned wake, reverse Kármán vortex (RKV) wake, and slanted reverse Kármán vortex (s-RKV) wake. Their presence in the $St-Re$ domain and representative flow structures are shown in figures 5 and 6. The steady wake is observed at $St \leq 0.6$ and $Re \leq 250$ (figures 6a, 5), where the wake is steady, similar to the flow structure behind a quiescent foil ($St = 0$). With a little increase in St and/or Re, the steady wake transmutes to q-KV wake (figure 6b) or q-RKV wake (figure 6c) representing a transition from a steady wake to a classical KV or RKV wake. The q-KV and q-RKV wakes form at low and high St, respectively, the former prevailing for smaller λ (≤ 1.0) only (figure 5). Here, Kármán or reverse Kármán vortices form immediately behind the foil while vanishing rapidly to generate a steady wake downstream (figures 6a-c). The generation of steady wake followed by Krmn wake was also found in the wake of a fixed elliptical cylinder at $Re = 100-150$ in Shi *et al.* (2020*a*) and Shi *et al.* (2020*b*). Depending on λ, when Re is further increased, KV wake forms, featuring negative and positive vortices above and below the foil symmetry line correspondingly (figure 6d). The 2S aligned wake refers to the case where both positive and

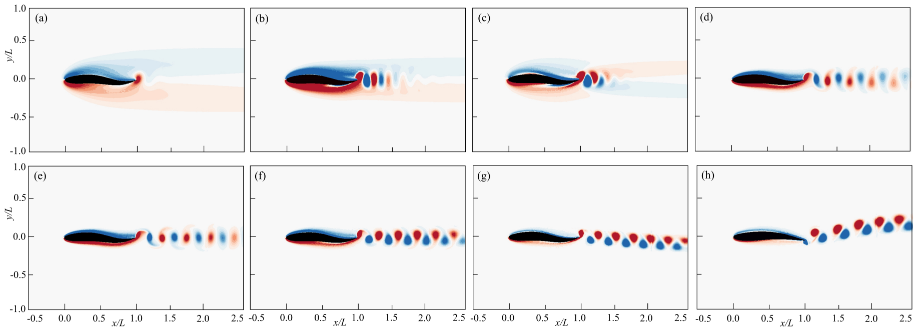

Figure 6. Typical instantaneous vorticity structures: (a) steady wake; (b) quasi Kármán vortex (q-KV) wake; (c) quasi reverse Kármán vortex (q-RKV) wake; (d) Kármán vortex (KV) wake; (e) 2S aligned wake; (f) reverse Kármán vortex (RKV) wake; (g) downward slanted reverse Kármán vortex (ds-RKV) wake; and (h) upward slanted reverse Kármán vortex (us-RKV) wake.

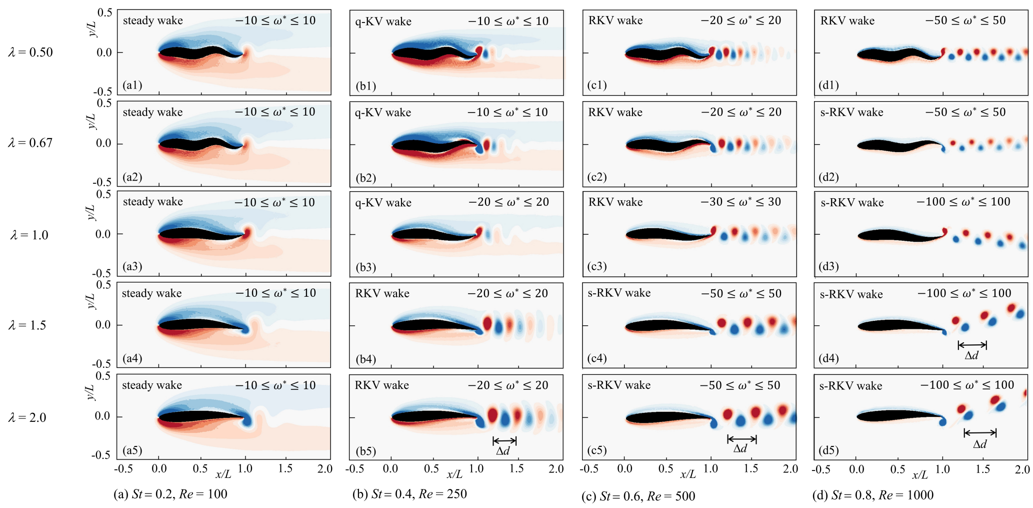

Figure 7. Contours of spanwise vorticity $\omega^* = \omega L/U$. The red and blue colors denote positive and negative ω^*, respectively.

negative vortices lie on the symmetric line (figure 6e). The 2S aligned wake is considered as the boundary between KV and RKV wakes, extensively discussed in the previous works (Godoy-Diana *et al.*, 2008, 2009; Marais *et al.*, 2012; Deng *et al.*, 2015, 2016; Andersen *et al.*, 2017; Chao *et al.*, 2019, 2021; Muhammad *et al.*, 2020). The emergence of 2S aligned wake at the KV-RKV boundary (red dash line) precedes the drag-thrust boundary (black solid line) in the St - Re map (figure 5). The same is true for a pitching foil (Godoy-Diana *et al.*, 2008). With a further increase in St and/or Re, RKV wake emerges, where the negative and positive vortices nestle oppositely to those of KV wake (figure 6f). In s-RKV wake, the symmetric line of two vortex streets does not coincide with the foil symmetric line. The slant direction can be upward or downward. The downward slanted RKV is referred to as ds-RKV wake (figure 6g) while upward slanted RKV refers to us-RKV wake (figure 6h). The slant direction of s-RKV wake is also affected by λ, see figure 6(g, h). Generally, the slant direction strongly depends on the first vortex pair generated by the foil (Zheng & Wei, 2012). Here, both ds-RKV and us-RKV wakes are considered as s-RKV wake because the physical mechanisms of the ds-RKV and us-RKV wakes are identical. The formation of the slanted wake is also common in flow-induced vibrations of cylinders (Bhatt & Alam, 2018).

Figure 5 also surfaces how λ affects the wakes behind a traveling wavy foil, particularly the transition between two different types of flow structures. For example, the KV-RKV wake transition bordered by 2S aligned wake advances with increasing λ. Similarly, RKV-s-RKV wake transition (blue dash-dotted line) also shifts to smaller St and/or Re when λ is increased. In addition, there is no s-RKV wake observed at λ = 0.50 (figure 5a). Physically, λ describes how the foil locomotion propagates from the leading to trailing edges. Therefore, the foils horizontal acceleration at the trailing edge declines with the decrease in λ. As a result, the convection velocity of the vortices with respect to U also decreases with declining λ. In the previous work, Godoy-Diana *et al.* (2009) showed that the generation of s-RKV wake is significantly dependent on the value of this convection velocity, where a larger value of this convection velocity may induce s-RKV wake. A smaller λ thus postpones the transition between RKV and s-RKV wakes.

EFFECT ON VORTEX STRENGTH

To evaluate quantitatively the influence of St, Re and λ on vortex strength at different regimes, figure 7 presents dimensionless spanwise vorticity ω^* $(= \omega L/U)$ structures at the four selected points located in the $St - Re$ plane (figure 5). The ω^* increases with St, Re and λ, which is consistent with the change in $\bar{C}_T$ in figure 2. A similar relationship of the spatial wavelength Δd with St, Re and λ is noticeable, having the same correspondence with $\bar{C}_T$. The growth of Δd with *St* and *Re* is ascribed to the increased velocity of vortices when *St* and *Re* are increased. On the other hand, it is easy to understand that a smaller λ would lead to a smaller velocity of vortices, hence a smaller Δd and $\bar{C}_T$.

CONCLUSION

A systematic numerical study is performed on hydrodynamic performance of a fish-like foil undergoing traveling wavy undulation for Strouhal number $St = 0.11.0$, Reynolds number $Re = 502000$, and non-dimensional wave length $\lambda = 0.502.0$ with the foil length keeping constant to replicate the native slender swimmer.

The time-mean thrust $\bar{C}_T$ is mapped on $St - Re$ plane for different λ values. A unifying mechanistic relationship of $\bar{C}_T$ with *St*, *Re* and λ is obtained as $\bar{C}_T = 0.36Re^{0.208}St^3\lambda - 6.13Re^{-0.6}$. The $\bar{C}_T$ enhances with increasing *St*, *Re* and λ. A predator-prey game at a sufficiently high Re relies on *St* and λ only as *Re* effect on $\bar{C}_T$ is negligible at a high *Re*. The unifying relationship also provides the scaling law of the drag-thrust boundary ($\bar{C}_T = 0$) that is marked as $St = 2.57Re^{-0.27}\lambda^{-1/3}$. An increase in λ advances the drag-thrust boundary to smaller *Re* and *St* values. The decreasing λ leads to a smaller fluctuation in thrust. A swimmer may have a more steady thrust when λ is smaller, consistent with the swimming behavior of the anguilliform swimmer. On the contrary, a larger λ enhances the maximum instantaneous thrust which explains why a slender swimmer adopts the C-start strategy during the survival behavior.

Seven distinct wake structures are identified, namely steady, q-KV, q-RKV, KV, 2S, RKV and s-RKV wakes. Among them, steady, q-KV, KV and 2S wakes are always drag producing while q-RKV and RKV wakes can produce both drag and thrust depending on λ. On the other hand, s-RKV wake is always thrust producing. When λ is smaller, s-RKV wake transmutes into RKV, hence s-RKV wake disappears at the λ = 0.50 examined. A smaller λ enhances the stability of the wake not to be slanted, deferring RKV-s-RKV wake boundary, KV-RKV wake boundary, and drag-thrust boundary.

REFERENCES

Alam, M.M. & Muhammad, Z. 2020 Dynamics of flow around a pitching hydrofoil. *Journal of Fluids and Structures* **99**, 103151.

Andersen, A., Bohr, T., Schnipper, T. & Walther, J. H. 2017 Wake structure and thrust generation of a flapping foil in two-dimensional flow. *Journal of Fluid Mechanics* **812**, R4.

Bhatt, R. & Alam, M.M. 2018 Vibration of a square cylinder submerged in a wake. *Journal of Fluid Mechanics* **853**, 301–332.

Bos, F. M., Lentink, D., Van Oudheusden, B. & Bijl, H. 2008 Influence of wing kinematics on aerodynamic performance in hovering insect flight. *Journal of Fluid Mechanics* **594**, 341–368.

Chao, L.-M., Alam, M.M., Ji, C. & Wang, H. 2021 Flow map of foil undergoing fast and slow pitching. *Physics of Fluids* **33**, 101902.

Chao, L.-M., Pan, G., Zhang, D. & Yan, G.-X. 2019 Numerical investigations on the force generation and wake structures of a nonsinusoidal pitching foil. *Journal of Fluids and Structures* **85**, 27–39.

Das, A., Shukla, R. K. & Govardhan, R. N. 2016 Existence of a sharp transition in the peak propulsive efficiency of a lowre pitching foil. *Journal of Fluid Mechanics* **800**, 307–326.

Deng, J., Sun, L. P. & Shao, X. M. 2015 Dynamical features of the wake behind a pitching foil. *Physics Review E* **92**, 063013.

Deng, J., Sun, L. P., Teng, L. B., Pan, D. Y. & Shao, X. M. 2016 The correction between wake transition and propulsive efficiency of a flapping foil: A numerical study. *Physics of Fluids* **92**, 094101.

Fish, F. E. & Lauder, G. V. 2006 Passive and active flow control by swimming fishes and mammals. *Annual Review of Fluid Mechanics* **38**, 193–224.

Gazzola, M., Argentina, M. & Mahadevan, L. 2014 Scaling macroscopic aquatic locomotion. *Nature Physics* **10**, 758–761.

Gazzola, M., Van Rees, M. & Koumoutsakos, P. 2012 C-start: optimal start of larval fish. *Journal of Fluid Mechanics* **698**, 5–18.

Godoy-Diana, R., Aider, J.-L. & Wesfreid, J. E. 2008 Transitions in the wake of a flapping foil. *Physics Review E* **77**, 016308.

Godoy-Diana, R., Marais, C., Aider, J.-L. & Wesfreid, J. E. 2009 A model for the symmetry breaking of the reverse benard-von karman vortex street produced by a flapping foil. *Journal of Fluid Mechanics* **622**, 23–32.

Gray, J. 1933 Studies in animal locomotion: I, the movement of fish with special reference to the eel. *Journal of Experimental Biology* **10**, 88–104.

Koochesfahani, M.M. 1989 Vortical patterns in the wake of an oscillating airfoil. *AIAA Journal* **27**, 1200–1205.

Marais, C., Thiria, J. E., Wesfreid, J. E. & Godoy-Diana, R. 2012 Stabilizing effect of flexibility in the wake of a flapping foil. *Journal of Fluid Mechanics* **710**, 659–669.

Muhammad, Z., Alam, M.M. & Noack, B. R. 2020 Efficient thrust enhancement by modified pitching motion. *Journal of Fluid Mechanics* **933**, A13.

Shi, X. Y., Alam, M. M. & Bai, H. L. 2020*a* Wakes of elliptical cylinders at low reynolds number. *Journal of Fluid Mechanics* **30**, 525–532.

Shi, X. Y., Alam, M. M., Bai, H. L. & Wang, H. 2020*b* The effect of reynolds number on the elliptical cylinder wake. *International Journal of Heat and Fluid Flow* **82**, 108553.

Zheng, Z. C. & Wei, Z. 2012 Study of mechanisms and factors that influence the formation of vortical wake of a heaving airfoil. *Physics of Fluids* **24**, 103601.